Synthesis and Efficient Visible Light Photocatalytic H$_2$ Evolution of A Metal-free g-C$_3$N$_4$/Graphene Quantum Dots Hybrid Photocatalyst

Jian-Ping Zou,[a] Lai-Chun Wang,[a] Jinming Luo,[b] Yu-Chun Nie,[a] Qiu-Ju Xing,[a] Xu-Biao Luo,[a] Hong-Mei Du,[a] Sheng-Lian Luo,[a,]* Steven L. Suib[c,]*

[a] *Key Laboratory of Jiangxi Province for Persistent Pollutants Control and Resources Recycle, Nanchang Hangkong University, Nanchang, Jiangxi, P. R. China*
[b] *Key Laboratory of Drinking Water Science and Technology, Research Center for Eco-Environmental Sciences, Chinese Academy of Sciences, Beijing, P. R. China*
[c] *Department of Chemistry, University of Connecticut, Storrs, CT, USA*

Abstract: In this work, we report a systematic study of the relationship between photocatalytic properties of hydrogen evolution and structures and morphologies of g-C$_3$N$_4$ prepared by different precursors (urea, melamine and dicyandiamide). The photocatalytic performances of H$_2$ production are affected by the method and degree of polymerization, the degree of protonation, and the morphology of g-C$_3$N$_4$ prepared by different precursors. Furthermore, a novel metal-free N-GQDs/g-C$_3$N$_4$ catalyst was designed and synthesized, which shows much better photocatalytic activity for H$_2$ evolution from water splitting than that of g-C$_3$N$_4$ due to the unique and multiple roles

* Corresponding author. E-mail: sllou@hnu.edu.cn (S.-L. Luo) or steven.suib@uconn.edu (S. L. Suib); Fax: +86 791 83953373 or +1 860 4862981.

of N-GQDs. A mechanism is put forth to explain the roles of N-GQDs and the detailed enhancement of photocatalytic performance of the N-GQDs/g-C_3N_4.

Kewords: Carbon nitride; Graphene quantum dots; Hydrogen evolution; Metal-free; Photocatalysis

1. Introduction

As fossil fuels are being rapidly consumed, human society is facing an energy crisis and environment issues [1,2]. Solar energy, an ultimate and green energy, could become an alternative for human dependence on conventional energy. Hydrogen is being vigorously pursued as a future energy carrier in the transition from the current hydrocarbon economy [3]. Despite the success of metals or metals oxides for photocatalysis applications, there remain some general problems. For example, most materials can only utilize UV light, and metals are relatively expensive, and readily cause environmental pollution [4]. Therefore, it is urgent to explore new metal-free catalysts with excellent visible-light-driven photocatalytic performance because metal-free catalysts are cheap and environmentally friendly.

Recently, graphitic carbon nitride (g-C_3N_4), a typical layered metal-free material, has been attracting intensive attention for its promising applications in water splitting and degradation of organic pollutants under visible light due to nontoxicity, reliable stability, and low cost [5,6]. These g-C_3N_4 materials could be used as good photoelectronic and photochemical anti-corrosive materials due to a suitable band gap [7]. However, like many other photocatalysts, g-C_3N_4 could suffer limited nonlocalized conductivity, high recombination rate, and low surface area, which might lead to overall low photocatalytic efficiency for water splitting [8-11]. Interestingly, the photocatalytic activities of g-C_3N_4 can be significantly improved by loading noble metals as a co-catalyst, such as Pt, Ru, Rh [12]. However, noble metals

2

are rare and expensive and mining them is harmful to the environment, which limits the large-scale applications of these catalysts [13-16].

Therefore, it is necessary to replace noble metals by earth abundant elements with durable and high efficiency in water splitting for hydrogen evolution [17]. Recently, fluorescent carbon nanodots (CDs) and graphene quantum dots (GQDs) have attracted much attention due to their unique properties and wide range of applications in photocatalysts and bioimaging fields [18,19]. After this, a few studies showed successful preparation of N and/or S doped GQDs with high electrocatalytic activity and conductivity for lithium batteries [20]. Interestingly, nitrogen-doped GQDs (N-GQDs) possessed excitation independent upconversion PL properties and much better absorption of visible and long-wavelength light than that of GQDs [21]. These results indicate that N-GQDs could act as a good co-catalyst for semiconductor catalysts.

Based on the above analysis, it is deserved to combine $g-C_3N_4$ with N-GQDs in order to obtain a novel metal-free composite catalyst with highly efficient photocatalytic H_2 evolution from water splitting under visible light irradiation. In addition, although there have been many reports on $g-C_3N_4$, there are few systematic reports on $g-C_3N_4$ materials prepared by different precursors and structure-function relationships. Thus, we tried to systematically investigate the structures, morphologies, and the hydrogen evolution properties of $g-C_3N_4$ synthesized by different inorganic precursors to make clear the effect of the method and degree of polymerization, degree of protonation, and morphology of $g-C_3N_4$ prepared by different precursors on the photocatalytic performances of H_2 production. In addition, the multiple roles of N-GQDs among the N-GQDs/$g-C_3N_4$ are clarified. The present work not only reports a novel metal-free catalyst with excellent photocatalytic performance but also opens a new avenue to study the relationships between

structures, morphologies, and photocatalytic properties of the g-C_3N_4 prepared under different conditions.

2. Experimental Section

2.1. Materials and Measurement

The samples were characterized by X-ray diffraction (XRD) for phase identification on a Bruker D8 ADVANCE diffractometer with Cu-Kα (λ=1.5406 Å) radiation. Ultraviolet-visible (UV-vis) diffuse reflection spectra were measured using a UV-vis U-3900H spectrophotometer. Brunauer-Emmett-Teller (BET) surface area measurements were performed with a micromeritics surface area analyzer at 77 K by using an adsorption apparatus. Fourier transformed infrared (FTIR) spectra were recorded using KBr pellets with a VERTEX-70 spectrometer. The morphology of the samples was investigated by scanning electron microscopy (SEM, FEI, Holland), transmission electron microscopy (JEM-2010HR), and high-resolution TEM (HRTEM) images. X-ray photoelectron spectroscopy (XPS) was obtained by using a VG 250 Escalab spectrometer equipped with an Al anode (Al-Kα = 1486.7 eV) as an X-ray source. Elemental analyses (C, N and H) were carried out with a Perkin-Elmer 2400 II elemental analyzer.

Electrochemical measurements were performed on a CHI 660D electrochemical workstation (Shanghai Chenhua, China) using a standard three-electrode cell with a working electrode, a standard calomel electrode as reference electrode, and a graphite electrode as counter electrode. The working electrodes were prepared by dip-coating: 10 mg of photocatalyst suspended in 5 mL anhydrous ethanol to produce stable suspension that was then dip-coated onto a 3 cm×1 cm fluorine-tin oxide (FTO) glass electrode, and the films drying under room temperature. The electrolyte (0.5 M Na_2SO_4) was purged with nitrogen. As for photocurrent measurements, a 300 W Xe

lamp was used as the source of simulated solar irradiation and the other conditions were similar to those of electrochemical measurements.

2.2. Syntheses

2.2.1. Syntheses of g-C$_3$N$_4$ from different precursors.

The chemicals are all analytical grade and used without further purification. A new method was proposed to synthesize g-C$_3$N$_4$. Typically, 6.5 g of urea was put into an alumina crucible with a cover and then heated to 550℃ in a muffle furnace for 2 h at a heating rate of 8℃·min^{-1}. After the reaction, the alumina crucible was cooled to room temperature, and a faint yellow powder was obtained. The resultant g-C$_3$N$_4$ was collected and ground into powder, and labeled as CN-U. Following the same procedure, g-C$_3$N$_4$ samples were also prepared by directly treating melamine and dicyandiamide, respectively. The resultant g-C$_3$N$_4$ obtained by melamine and dicyandiamide was denoted as CN-M and CN-D, respectively.

2.2.2. Syntheses of N-GQDs.

N-GQDs were synthesized according to the method reported in the literature [22]. Typically, 0.5254 g (2.5 mmol) citric acid and 0.6006 g (10.0 mmol) urea were dissolved in 12 mL deionized water, and stirred to form a clear solution. Then the solution was transferred into a 50 mL Teflon lined stainless steel autoclave. The sealed autoclave was heated to 160 ℃ in an electric oven and kept for 8 h. The final product was collected by adding ethanol into the solution and centrifuged at 5000 rpm for 5 min. The solid can be easily redispersed into water.

2.2.3. Syntheses of N-GQDs/CN-U.

In a typical preparation, 0.1 g of CN-U was added into 10 mL water, after ultrasonic stirring for 1 h at room temperature. Stoichiometric N-GQDs was added to the as-obtained CN-U solution, and magnetically stirred for another 30 min. The

resulting solid were collected by filtration, and dried at 75℃. The obtained gray powder is denoted as N-GQDs/CN-U nanocomposites. Hereafter, the N-GQDs/CN-U containing 3%, 5%, 10%, 15%, and 20% (at.%) N-GQDs are denoted as 3N-CNU, 5N-CNU, 10N-CNU, 15N-CNU, and 20N-CNU, respectively.

2.3. Photocatalytic activity for water splitting

Photocatalytic activities of the g-C_3N_4 synthesized by different precursors and the hybrid N-GQDs/CN-U with different loadings of N-GQDs were investigated. All photocatalytic H_2 evolution experiments were carried out in a Pyrex glass reaction cell connected to a closed gas-circulation and evacuation system (Prefect Light, Beijing, Labsolar-III (AG), as shown in Figure S1). About 0.02 g photocatalyst was dispersed in 80 mL of aqueous solution (containing 10 vol.% triethanolamine as a sacrificial agent). Then 3% Pt was loaded onto the samples surface by photodeposition of H_2PtCl_6. The suspension was evacuated several times to completely remove air and irradiated by a 300 W Xe-lamp (Perfect light PLS-SXE300C). A cutoff filter was employed to achieve visible-light ($\lambda > 420$ nm) irradiation. The amount of hydrogen evolution from photocatalytic splitting water was analyzed by using an online gas chromatograph with a thermal conductive detector (TCD) and a capillary column (5 Å molecular sieve). High purity argon gas was used as a carrier gas. During the test, the temperature of the reaction solution was maintained at 6 ℃ by a flow of cooling water.

3. Results and Discussion

3.1. Systematic research on g-C_3N_4 prepared by different precursors

Since the photocatalytic properties of g-C_3N_4 are affected by the synthesis conditions and structure, herein, we presented a systematic study of the structures,

morphologies, and the photocatalytic properties of g-C_3N_4 synthesized by different inorganic precursors. In our experiment, g-C_3N_4 was prepared by directly heat treating urea, melamine, and dicyandiamide under the same conditions (550℃, 2 h in air).

The morphologies and microstructures of CN-U, CN-D and CN-M were investigated by SEM and TEM. As shown in Figure 1, all the samples consist of large amounts of packing layers with different sizes of nanosheets. CN-U favors the formation of thin nanosheets with porous structure, while CN-D and CN-M tend to form thick layered structures, which indicates that the morphologies and microstructures of the resultant g-C_3N_4 strongly depend on the precursors containing different heteroatoms.

Figure 2a shows the X-ray diffraction (XRD) patterns of the as-prepared g-C_3N_4. All of the samples have two characteristic peaks. The weak peak at 13.1º is indexed as (100), while the strong peak at about 27.5º is indexed as (002). The two diffraction peaks are in good agreement with the g-C_3N_4 reported in the literature [23]. Further observation shows that the (002) characteristic peaks occur at 27.43º, 27.48º and 27.54º for CN-M, CN-D and CN-U, respectively. The results indicate that O-containing precursors (urea) can improve the polycondensation and more compact structures of g-C_3N_4 can be obtained with urea than with the other two precursors [24]. As shown in Table 1, the surface areas of CN-U, CN-D and CN-M are 77 $m^2 \cdot g^{-1}$, 16 $m^2 \cdot g^{-1}$, and 9.0 $m^2 \cdot g^{-1}$, respectively. CN-U has the largest pore volume. The above results indicate that different precursors will result in different types of polymerization and finally lead to different morphology frameworks and different surface areas of g-C_3N_4.

As shown in Figure 2b, all the samples exhibit excellent visible light absorption with absorption edges around 500 nm, and the absorption edges of the samples

apparently shift to longer wavelengths from CN-U to CN-M, which could be due to the different local structures and morphologies of the as-synthesized g-C$_3$N$_4$ samples. And the energy gap (E$_g$) of the different g-C$_3$N$_4$ samples can be estimated from the intercept of the tangents to the plots of (Ahυ)$^{1/2}$ versus photo energy (Figure 2(b)), showing the E$_g$ values of CN-D, CN-M, and CN-U are 2.66, 2.67 and 2.80 eV, respectively. In principle, the g-C$_3$N$_4$ sample with larger energy gap exhibits better redox ability of its charge carriers, which could result in better photocatalytic performance. As shown in Figure 2c, obvious anodic photocurrents are generated by the g-C$_3$N$_4$ photoelectrodes, indicating the efficient generation and separation of photoinduced electron-hole pairs within similar electrolyte interfaces. The CN-U material produces the largest photocurrents among the three samples, due to better condensation and enlarged surface area, which are favorable for charge collection and separation at interfaces. From Figure 2d, the CN-U material exhibits the best photocatalytic activity for hydrogen production under visible light irradiation among the as-prepared catalysts. The rate of hydrogen evolution of CN-U is 8.2 times that of CN-M and 6.3 times that of CN-D, respectively.

To explain why the different precursors, structures, and morphologies of g-C$_3$N$_4$ lead to different photocatalytic performances of H$_2$ production, we carried out the following experiments and characterization studies. As shown in Figure 3a, there are five characteristic peaks at 810, 1245, 1324, 1458, and 1632 cm^{-1} among the three kinds of g-C$_3$N$_4$, which are attributed to the skeletal vibrations of tri-s-triazine ring units (C$_6$N$_7$, Figure S3a).The signal at 1410 cm^{-1} originates from the stretching vibrations of s-triazine ring units (C$_3$N$_3$, Figure S3b) [25]. These results indicate that s-triazine and tri-s-triazine ring units simultaneously exist in the g-C$_3$N$_4$ prepared by three different precursors. X-ray photoelectron spectroscopy (XPS) was used to

determine the bonds and structures of the samples (Figure 3b-d). In all samples, the typical C 1s and N 1s peaks were observed. The peak at 399.6 eV is assigned to the tertiary N bonded to carbon atoms in the form of $N-(C)_3$. The weak peak with a high binding energy at 401.1 eV can be attributed to $C-NH_x$ in the aromatic cycles (see Supporting Information for more details) [26,27].

In addition, carbon and nitrogen contents of the samples were determined by elemental analyses. As shown in Table 1, the order of C/N molar ratio of the three kinds of g-C_3N_4 is CN-U <CN-D <CN-M, which indicates the order of molar ratio of tri-s-triazine/s-triazine ring units (C_6N_7/C_3N_3) is CN-U>CN-D>CN-M. The tri-s-triazine ring unit is more stable than the s-triazine ring unit, which results in the photocatalytic activity of H_2 evolution of g-C_3N_4 composed of tri-s-triazine ring units is much better than that of g-C_3N_4 composed of s-triazine ring units [28]. In addition, the C/N molar ratios of g-C_3N_4 synthesized by three different precursors are all lower than the theoretical value of 0.75 for g-C_3N_4, which could also be due to the existence of many amino groups ($C-NH_x$, Figure S3c) in the as-prepared g-C_3N_4. More functional amino groups mean more protonation or defects in g-C_3N_4, which finally results in poor photocatalytic activity of g-C_3N_4 [29]. Furthermore, the experimental result (Figure 2d) that the hydrogen production rate increases with a decrease of the C/N molar ratio of g-C_3N_4 confirms the results of FTIR, XPS, and elemental analyses. Therefore, different precursors will lead to different types and degrees of polymerization, different degrees of protonation, different morphologies, and different energy gap, and then finally give rise to different photocatalytic performances of g-C_3N_4.

Furthermore, in order to confirm the process of polymerization, we investigated urea-derived g-C_3N_4 calcinated at different times. As shown in Figure S4, the

crystallinity becomes better and the crystal structure of g-C_3N_4 gradually transfers from s-triazine (metastable state) to tri-s-triazine (stable state) ring units with an increase of calcination time, and finally there is simultaneous existence of tri-s-triazine and s-triazine ring units in g-C_3N_4. Because the structure of g-C_3N_4 is composed of different units (tri-s-triazine or s-triazine ring units) and can not be well distinguished by XRD, the C/N molar ratio of g-C_3N_4 is an important method. As shown in Table S1, the C/N molar ratio of g-C_3N_4 decreases with the calcination time but is lower than the theoretical value of 0.75 for g-C_3N_4, which demonstrates the above analysis of the method of polymerization (or transition of secondary structure units) of g-C_3N_4. Furthermore, this analysis of the method of polymerization of g-C_3N_4 can be confirmed by the photocatalytic results in Table S1 that the photocatalytic activity of H_2 production increases with an increase of calcination time. Therefore, the type and degree of polymerization, as well as the degree of protonation of g-C_3N_4 can effectively affect its photocatalytic activity.

3.2. Photocatalytic performance of N-GQDs/g-C_3N_4

Because g-C_3N_4 still has some disadvantages, such as weak visible light absorption and high recombination rate of photo-generated electrons and holes, we tried to combine g-C_3N_4 with N-GQDs to form N-GQDs/g-C_3N_4 in order to markedly improve the photocatalytic performance of g-C_3N_4. The results of XRD (Figure S5) and FTIR (Figure S6) spectra of N-GQDs/CN-U are similar to that of CN-U, showing that the coupling of N-GQDs with CN-U does not destroy the structure of CN-U. Figure 4a shows TEM images of N-GQDs/CN-U. Well dispersed N-GQDs (marked with black dots) with mean diameters of 2~6 nm are embedded in the porous CN-U matrix surfaces. HRTEM images (Figures 4b and S7) clearly reveal good crystallinity of the N-GQDs with a lattice spacing of 0.238 nm, corresponding to the (1120) lattice

fringes of nitrogen doped grapheme [30]. The results of XPS also demonstrate that N-GQDs is loaded on the surface of CN-U (Figure S8). The photocatalytic H_2 evolution rate of N-GQDs/CN-U with different N-GQDs loadings are shown in Figure 4c. The CN-U exhibits photocatalytic activity with a H_2 evolution rate of 1.01 mmol·h^{-1}·g^{-1}, and after loading with N-GQDs, the H_2 evolution rate of CN-U is significantly improved. The 15N-CNU material shows the best photocatalytic activity among the as-prepared samples and the H_2 production rate of 15N-CNU is 2.18 mmol·h^{-1}·g^{-1} which is about 2.16 times of the CN-U with a quantum efficiency at 420 nm of 5.25%. The results demonstrate that N-GQDs can effectively enhance the visible light driven photocatalytic activity of CN-U.

Figure 4d shows the UV-vis absorption spectra of CN-U and 15N-CNU. Compared with the CN-U, the 15N-CNU shows better absorption intensity in the visible region and the absorption edge of the 15N-CNU occurs with a marked red-shift due to the electronic coupling and quantum effect of N-GQDs. The CN-U and 15N-CNU exhibit band gasp of ca. 2.80 and 2.72 eV, respectively. Photocurrent responses of the CN-U and 15N-CNU were investigated for several on-off cycles under visible light irradiation. Figure 4e shows the transient photocurrent responses via two on-off cycles of CN-U and 15N-CNU electrodes under visible light irradiation. The photocurrent value of 15N-CNU electrode is about 2 times higher than that of the CN-U electrode. To further explain the optical properties of the N-GQDs/CN-U, a detailed PL study was carried out by using different excitation wavelengths. As shown in Figure 4f, N-GQDs exhibit good upconversion properties. When excited by 600~800 nm light, short wavelength light in the range of 400 to 600 nm is generated, which is attributed to a multiphoton active process similar to the reported carbon dots [31]. The upconversion PL property of N-GQDs markedly improves the light absorption of CN-

U. In addition, we did the experiments of photocatalytic hydrogen evolution under long wavelengths irradiation by using a 590 nm cut-off filter. As shown in **Figure S9**, there is no hydrogen detected for CN-U and N-GQDs, whereas the photocatalytic hydrogen evolution rate of 10N-CNU, 15N-CNU and 20N-CNU is 8.00, 13.30 and 10.31 $\mu mol \cdot g^{-1} \cdot h^{-1}$, respectively, under long wavelengths irradiation ($\lambda > 590$ nm). The results confirm the CN-U can utilize NIR light for photocatalytic H_2 evolution after the addition of N-GQDs.

3.3. Possible photocatalytic mechanism

On the basis of the above experimental results, a mechanism for the photocatalytic H_2 production on N-GQDs/CN-U is proposed. As shown in Scheme 1, under irradiation of visible light, CN-U can directly absorb light of 420~470 nm and generate electrons (e^-) and holes (h^+). Meanwhile, N-GQDs can absorb visible light (600-800 nm) and then emit short wavelength light ($\lambda < 470$ nm) that is absorbed by CN-U to generate electrons (e^-) and holes (h^+). The electrons are excited from the VB to CB of CN-U, and then transferred to the surface of N-GQDs, whereas the holes in the VB react with sacrificial regents. Therefore, there is effective charge separation and the separated electrons have enough time to reduce H_2O (or H^+) to H_2 on the surface of N-GQDs. This mechanism explains the multiple roles of N-GQDs in the N-GQDs/CN-U composite and why the N-GQDs/CN-U exhibits much better activity for hydrogen evolution than that of CN-U.

4. Conclusions

We systematically investigated the structures, morphologies and photocatalytic properties of the g-C_3N_4 prepared by three precursors (urea, melamine and dicyandiamide) and clarified the relationship of structure-function. Different precursors result in differences of the types and degrees of polymerization, the degree

of protonation, and morphologies of g-C_3N_4, and how they affect the photocatalytic performances of g-C_3N_4. In addition, metal-free N-GQDs/CN-U nanocomposites were synthesized by a facile method in order to improve the photocatalytic performance of g-C_3N_4. Experimental results show that 15N-CNU has the best photocatalytic activity with a H_2 evolution rate of 2.18 mmol·h^{-1}·g^{-1} (2.16 times of CN-U), and the quantum efficiency at 420 nm is 5.25%. A mechanism was proposed to explain the multiple roles of N-GQDs in the N-GQDs/CN-U composite and why the N-GQDs/CN-U exhibits much better activity for H_2 evolution than that of CN-U.

Appendix A. Supplementary data

The detailed analyses of XPS, FTIR, and specific surface area, pore volume and pore size and the calculation of quantum efficiency, XRD and FTIR results of N-GQDs/g-C_3N_4 and g-C_3N_4 calcinated at different times with the precursor of urea, XPS and HRTEM results of 15N-CNU, as well as the physicochemical properties of urea-derived g-C_3N_4 synthesized at different calcination time are available free of charge via http://www.sciencedirect.com.

References

[1] F. E. Osterloh, Chem. Soc. Rev. 42 (2013) 2294-2320.

[2] Y. Qu, X. Duan, Chem. Soc. Rev. 42 (2013) 2568-2580.

[3] M. S. Dresselhaus, I. L. Thomas, Nature. 414 (2014) 332-337.

[4] K. Maeda, T. Takata, M. Ha, N.Saito, K. J. Domen, Am. Chem. Soc. 127 (2005) 8286-8287.

[5] X. C. Wang, K. Maeda, A. Thomas, K. Takanabe, G. Xin, J. M. Carlsson, Nat. Mater. 8 (2009) 76-80.

[6] Y. Wang, X. C. Wang, M. Antonietti, Angew. Chem. Int. Ed. 51 (2012) 68-69.

[7] Y. Wang, R. Shi, J. Lin, Y. Zhu, Sci. 4 (2012) 2922-2929.

[8] M. G. Walter, E. L. Warren, J. R. McKone, S. W. Boettcher, Q. Mi, E. A. Santori, N. S. Lewis, Chem. Rev. 110 (2012) 6446-6473.

[9] N. Z. Bao, L. M. Shen, T. Takata, K. Domen, Chem. Mater. 20 (2008) 110-117.

[10] H. Yan, J. Yang, G. Ma, G. Wu, X. Zong, Z. Lei, J. Shi, C. Li, J. Catal. 266 (2009)165-168.

[11] Y. D. Hou, A. B. Laursen, J. S. Zhang, Y. S. Zhu, Angew. Chem. Int. Ed. 52 (2013) 3621-3625.

[12] C. Kong, S. X. Min, G. G. Lu, ACS Catal. 4 (2014) 2763-2769.

[13] M. Moriya, T. Minegishi, H. Kumagai, M. Katayama, J. Kubota, K. J. Domen, J. Am. Chem. Soc. 135 (2013) 3733-3735.

[14] J. Zhou, G. H. Tian, Y. J. Chen, X.Y. Meng, Y. S. Shi, X. C. Rui, K. Pan, H. G. Fu, Chem. Commun. 49 (2013) 2237-2239.

[15] S. R. Lingampalli, U. K. Gautam, C. N. R. Rao, Energy Environ. Sci. 6 (2013) 3589-3594.

[16] A. Tanaka, K. Hashimoto, H. Kominami, J. Am. Chem. Soc. 136 (2014) 586-589.

[17] Y.Qu, W. Zhou, Z. U. Ren, S. C. Du, X.Y. Meng, G. H. Tian, K. Pan, G. F. Wang, H. G. Fu, J. Mater. Chem. 22 (2012) 16471-16476.

[18] S. N. Baker, G. A. Baker, Angew. Chem. Int. Ed. 49 (2010) 6726-6744.

[19] H. Li, Z. Kang, Y. Liu, S. T. Lee, J. Mater. Chem. 22 (2012) 24230.

[20] Y. Li, Y. Zhao, H. Cheng, Y. Hu, G. Shi, L Dai, L. Qu, J. Am. Chem. Soc. 134 (2012) 15-18.

[21] D. Qu, M. Zheng, P. Du, Y. Zhou, Y. G. Zhang, H. Q.T an, Z. C. Sun, Nanoscale. 5 (2013) 12272-12277.

[22] D. J. Jiang, Y. Zhang, H. Y. Chu, J. Liu, J. Wan, M. Chen, RSC Adv. 4 (2014) 16163-16171.

[23] Y.J. Cui, Z. X. Ding, X. Z. Fu, X. C. Wang, Angew. Chem. Int. Ed. 51 (2012) 11814-11818.

[24] W.D. Zhang, Q. Zhang, F. Dong, Z. W. Zhao, INT. J. Photoenergy. 1 (2013) 685038

[25] L. Ge, Mater. Lett. 65 (2011) 2652-2654.

[26] B. Jurgens, E. Rran, J. Senker, P. Kroll, H. Muller, W. Schnick, J. Am. Chem. Soc. 125 (2003) 10288-10300.

[27] V. N. Khabashesku, J. L. Zimmerman, J.L. Margrave, Chem. Mater. 212 (2000) 3264-3270.

[28] E. Kroke, M. Schwarz, E. Horath-Bordon, P. Kroll, B. Noll, A. D. Norman, New J. Chem. 26 (2002) 508-512.

[29] D. J. Martin, K. Qiu, S. A. Shevlin, A. D. Handoko, X. Chen, Z. Guo, J. Chem. Int. Ed. 53 (2014) 9240-9245.

[30] Y. Ju, W. Chen, Biosens. Bioelectron. 58 (2014) 219-225.

[31] H.T. Li, X. D. He, Z. H. Kang, H. Huang, Y. Liu, J. L. Liu, S. Y. Lian, C. H. Tang, X. B. Yang, S. T. Lee, Angew. Chem. Int. Ed. 49 (2010) 4430-4434.
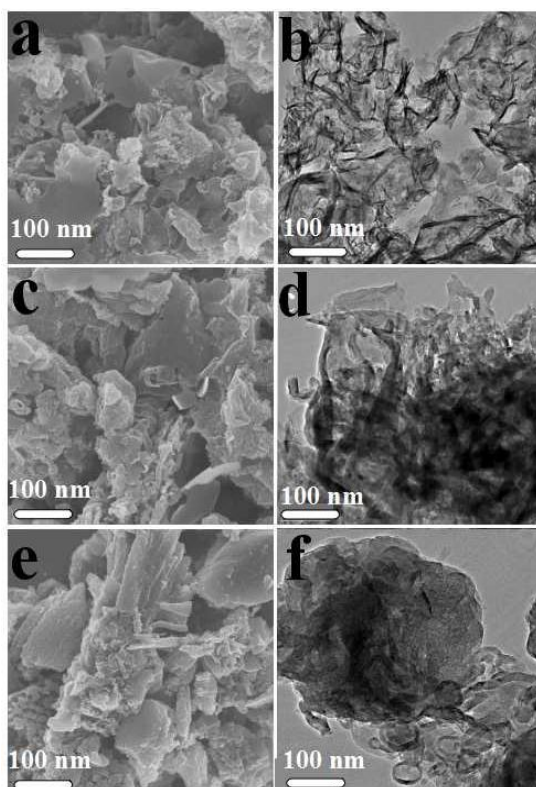
Figure 1. SEM and TEM images of CN-U (a and b), CN-D (c and d), and CN-M (e and f), respectively.
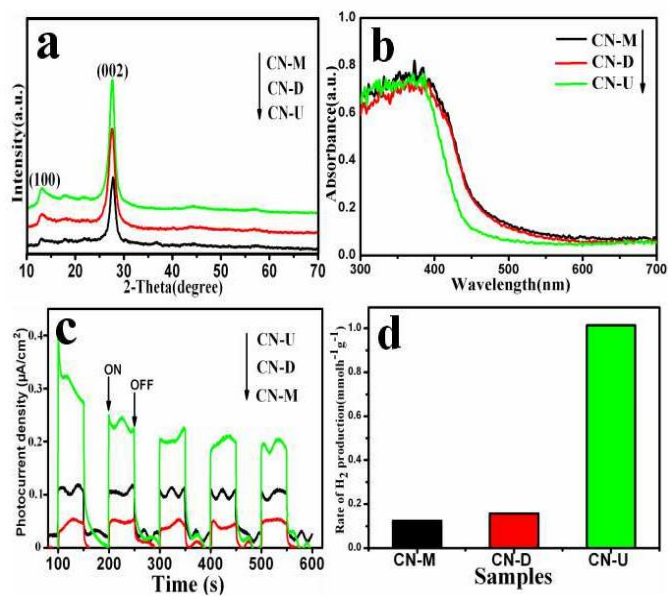

Figure 2. XRD patterns (a); UV-vis absorption spectra (b); Photocurrent curves (c) and Photocatalytic hydrogen production rate (d).
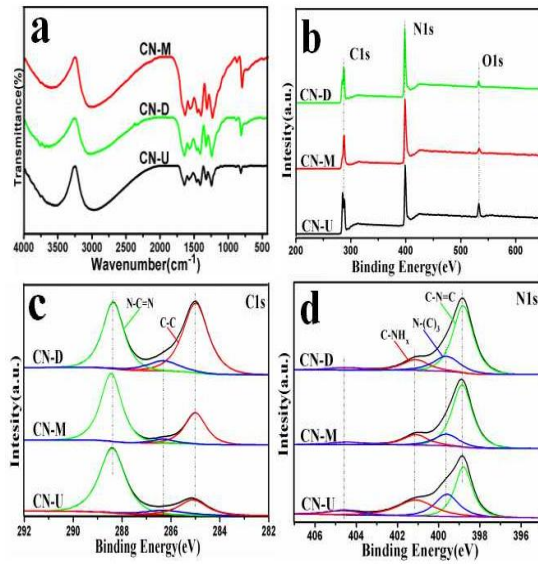
Figure 3. FTIR spectra of g-C_3N_4 (a); XPS survey spectra of g-C_3N_4 (b); High-resolution XPS of spectra of C 1s (c) and N 1s (d) of the three kinds of g-C_3N_4.
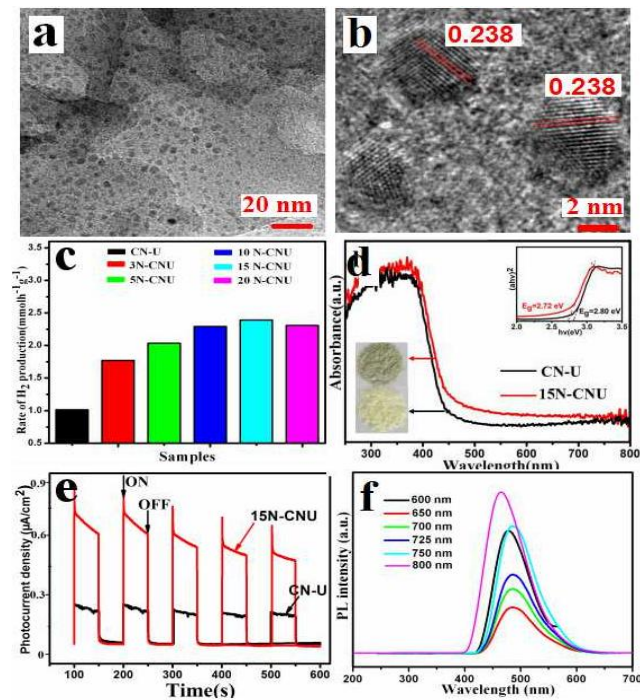

Figure 4. TEM images (a) and HRTEM images (b) of the as-synthesized 15N-CNU; The rate of hydrogen evolution over N-GQDs/CN-U with different amounts of N-GQDs under the irradiation of visible light using triethanolamine as sacrificial reagent (c); UV-visible absorption spectra of CN-U and 15N-CNU catalysts (The inset shows the intersection value is the band gap) (d); Transient photocurrent curves of CN-U and 15N-CNU (e) ; The upconversion PL spectra of N-GQDs irradiated under 600~800 nm light (f).
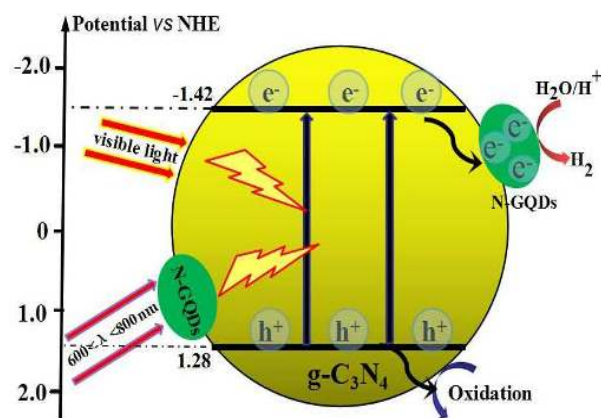
Scheme 1. Proposed photocatalytic mechanism for hydrogen evolution over N-GQDs/CN-U under visible light irradiation.

Table 1. Summary of the physicochemical properties of the g-C_3N_4 synthesized by different precursors.

Sample	Band edge [eV]	BET [$m^2 \cdot g^{-1}$]	HER rate [$mmol \cdot h^{-1} \cdot g^{-1}$]	Molar ratio C/N
CN-U	2.80	77.04	1.0141	0.661
CN-D	2.66	16.11	0.3853	0.671
CN-M	2.67	9.42	0.3411	0.678